Mixed Conductive Composites for 'Low-Temperature' Thermo-chemical CO2 Splitting and Syngas Generation

Journal:	*Journal of Materials Chemistry A*
Manuscript ID	TA-ART-03-2020-003232.R1
Article Type:	Paper
Date Submitted by the Author:	23-May-2020
Complete List of Authors:	Jiang, Qiongqiong; North Carolina State University, Chemical Engineering; Institute of Engineering Thermophysics Chinese Academy of Sciences Gao, Yunfei; North Carolina State University, Chemical Engineering Haribal, Vasudev; North Carolina State University, Chemical and Biomolecular Engineering Qi, He; West Virginia University, Mechanical & Aerospace Engineering Department Liu, Xingbo; West Virginia University, Department of Mechanical and Aerospace Engineering Hong, Hui; Chinese Academy of Sciences Jin, Hongguang; Institute of Engineering Thermophysics, Chinese Academy of Sciences Li, Fanxing; North Carolina State University, Chemical Engineering

Journal of Materials Chemistry A

Mixed Conductive Composites for 'Low-Temperature' Thermochemical CO_2 Splitting and Syngas Generation

Qiongqiong Jiang[# a, b, c], Yunfei Gao[# a], Vasudev Pralhad Haribal [a, b], He Qi [d], Xingbo Liu [d], Hui Hong[b, c], Hongguang Jin[b, c], Fanxing Li [a, *]

An effective strategy to design platinum group metal (PGM) free redox catalysts for "low temperature" CO_2 splitting followed with methane partial oxidation was proposed and validated. Composites of mixed ionic-electronic conductive (MIEC) oxides were found to be highly effective at relatively low temperatures (600 – 750 °C). Specifically, perovsktie structured $LaNi_{0.35}Fe_{0.65}O_3$ and rock salt structured $Ce_{0.85}Gd_{0.1}Cu_{0.05}O_{2-\delta}$, as two compatible yet structurally distinct MIEC oxides, were integrated into composite redox catalyst particles. Resulting from the synergistic effect of the two MIEC phases, 90% CO_2 to CO conversion was demonstrated at 750 °C. Up to 90% methane conversion with 96% CO selectivity was also achieved in the methane POx step. The redox catalysts were characterized in detail to illustrate the underlying mechanisms for the synergistic effects. Electrical conductivity relaxation (ECR) measurements indicated significantly lowered activation energy for lattice oxygen (O^{2-}) migration (0.43 eV). The enhanced oxygen migration in turn led to reversible exsolution of active transition metal nanoparticles (Ni-Fe alloy) from the mixed oxide, serving as active sites for methane activation while further enhancing lattice oxygen exchange, as confirmed by in-situ X-ray diffraction and transmission electron microscopy. As a result, the composite redox catalysts demonstrate superior redox activity, coke resistance, and long term redox stability, making them potentially suitable for CO_2 utilization and methane partial oxidation under a hybrid redox process scheme.

1. Introduction

Owing to the increasing greenhouse gas (GHG) emission from fossil fuels, global climate change has become a worldwide concern. Carbon dioxide (CO_2), as the leading GHG, is a major contributor to the environment-instability and ecosystem-imbalance[1]. CO_2 emissions have grown to 43 billion metric tons (bmt) in 2019, far exceeding the target of 20 bmt by the year 2040 according to the Paris Agreement[2]. Meanwhile, the global demand for energy, especially fossil fuels, is still on the rise with a projected average of 1.4% increase each year through 2035 [3]. Carbon capture and storage (CCS) can reduce CO_2 emissions from fossil fuel combustion. However, most CCS technologies, including pre-combustion, oxy-fuel combustion and post-combustion, are energy and capital intensive[4].

With the aim to address both environmental and energy challenges, novel CO_2 utilization techniques are highly desirable to potentially improve the economic attractiveness for CO_2 management while reducing emissions[5]. Repurposing CO_2 from industrial flue gases and efficiently converting the CO_2 into value-added chemicals, which are often less energy-intensive to produce, is particularly promising.

The technologies to convert CO_2 into chemicals can be divided into electrochemical, photochemical, and thermochemical approaches[6]. These approaches face different challenges. The feasibility of electrochemical reduction of CO_2 relies on electrocatalysts that can reduce CO_2 at low overpotentials, high current densities and have favorable selectivity as well as long lifetime[7]. Despite the current rapid progress, electrocatalysts reported to date have yet to meet these stringent requirements. Photoelectrochemical reduction of CO_2, discovered by Halmann[8], faces challenges such as self-photocorrosion of the semiconductor materials, charge recombination, and performance

a. North Carolina State University, Chemical and Biomolecular Engineering, USA.
b. Institute of Engineering Thermophysics, Chinese Academy of Sciences, China.
c. University of Chinese Academy of Sciences, Beijing 100049, China.
d. West Virginia University, Mechanical and Aerospace Engineering, USA
co-first authors;   E-mail: fli5@ncsu.edu.

limitations of the photocatalysts[9]. CO_2 can also be thermochemically converted using an oxide-based redox catalyst, also known as an oxygen carrier, at elevated temperatures facilitated by concentrated solar energy[10]. Although significant progress has been made in the development and optimization of the redox materials for thermochemical CO_2-splitting, the high operating temperature (>1100 °C) and limited CO_2 conversion remain as key challenges for these processes[9]. To address these barriers, we proposed an open-loop Hybrid Redox Process (HRP) concept for 'low-temperature' thermochemical reduction of CO_2 (**Fig. 1**)[11].
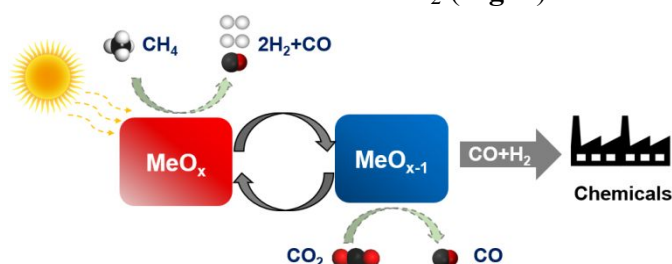
Fig. 1 Schematic diagram of the hybrid redox processes (HRP).

In HRP, the thermochemical reduction of CO_2 is facilitated by an oxide-based redox catalyst, shown in Eq. 1. In this step, the redox catalyst, in its reduced form, reacts with CO_2 to replenish its lattice oxygen while producing CO. The re-oxidized redox catalyst is then reacted with methane (Eq. 2) to form syngas with ~2:1 ratio of H_2: CO. The use of methane as the reducing agent not only lowers the operating temperature for the CO_2-splitting cycle but also provides a valuable syngas product for chemical production[12].

$$CO_2 + MeO_{x-1} = MeO_x + CO \qquad 1$$

$$CH_4 + MeO_x = Me_{x-1} + CO + 2H_2 \qquad 2$$
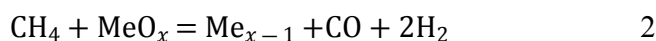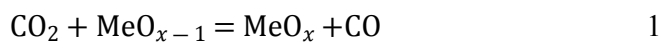
For thermochemical redox cycles, the performance of the redox catalysts is one of the most critical factors affecting the overall process performance. Extensive research has been conducted for redox catalyst development and optimization in the context of CO_2-splitting. In terms of its active (oxygen-carrying) component, oxides and mixed oxides of Fe, Co, and/or Ni have been investigated as suitable candidates[13]. Veser et al. [14] investigated chemical looping dry reforming (CLDR) using nanostructured $Fe@SiO_2$ and Fe–BHA (barium hexa-aluminate) with high specific surface area ($225 m^2g^{-1}$), and Fe-BHA showed higher redox kinetics and stability compared to $Fe@SiO_2$ due to a partial loss of the core-shell structure and formation of silicates for the latter, at about 800°C.

To enhance the redox performance of iron oxides, iron-nickel mixed oxides were tested, showing high methane and CO_2 conversions of about 90% for CLDR at ~1000 °C[15]. Besides these first-row transition metal oxides, ceria-based oxides were also explored as the oxygen-carrying medium, achieving 95% CO_2 conversion in the CO_2-splitting step at 800°C. However, the observed syngas yield was limited to 38% due to the relatively low selectivity[16]. Although promising results were obtained, the operating temperatures required for the abovementioned oxygen carriers are relatively high with limited CO_2 conversion and/or syngas yield. The high operating temperature requirement is particularly problematic for CO_2 utilization since it poses significant challenges over heat integration, reactor materials of construction and operation, and coke formation[17]. Recent experimental and density functional theory (DFT) studies indicate that perovskites, with a general formula ABO_3[18], possess high oxygen vacancy conductivities that are desirable for these redox reactions[19]. Ronald et al. [20] demonstrated the ability of $La_{0.6}Sr_{0.4}Co_{0.2}Fe0.8O_{3-\delta}$ (LSCF) to perform dry reforming of methane (DRM) in a membrane reactor in a temperature range of 840°C-1030°C. Zhang et al. [11c] reported platinum group metal (PGM)-free nanocomposites $Sr_3Fe_2O_{7-\delta}$ which showed near 100 % conversion for both CH_4 and CO_2 and ~96% syngas selectivity at 950°C.

The operating temperature of HRP is primarily dictated by the requirement for methane activation. As the most stable hydrocarbon molecule, the C-H

bond in methane is difficult to activate. This is especially the case in the proposed redox approach where lattice oxygen species, which can be significantly less active than gaseous oxidants, are used for methane activation. Previous research indicated that the use of PGMs as promoters (or active catalytic sites) on perovskite-based redox catalysts facilitates effective methane activation at low temperatures[10d, 21]. The same principles apply to ceria-based redox catalysts. Haribal et al. [11b] reported Rh promoted, lanthanum doped cerium oxide which achieved near-complete CO_2 conversion with 83% syngas yield at 650°C.

Although PGMs can effectively reduce the temperature for methane activation, their costs can be prohibitive. To our knowledge, however, non-PGM containing redox catalysts have yet to demonstrate satisfactory CO_2 and methane conversions at $\leq$ 750 °C. In the current study, we enhance the redox catalysts' activity for methane activation and CO_2 splitting in the absence of PGM via (i) facilitating lattice oxygen removal and replenishment by enhancing the bulk conductivity for O^{2-} and electrons; (ii) promoting the surface catalytic activity of the redox catalysts through dynamic exsolution of active transition metals on the oxide surface. The above functions are realized by composites of two mixed-conductive oxides with distinct structures, i.e., $Ce_{0.85}Gd_{0.1}Cu_{0.05}O_{2-\delta}$ (CGCO) and $LaNi_{0.35}Fe_{0.65}O_3$ (LNF), which demonstrated high activity at relatively low operating temperatures (≤750°C). Resulting from the unique properties of the composite redox catalysts, up to 90% CO yield and 96% syngas selectivity were demonstrated at 750 °C. *In-situ* XRD, TEM, EDX, and CO-chemisorption were utilized to elucidate the underlying mechanisms for HRP catalysts in both the methane partial oxidation (POx) and CO_2 splitting steps.

2. Experimental

2.1 Synthesis of the mixed conductive composites

CGCO and LNF were separately prepared via a modified sol-gel method. Nitrate precursors, i.e., $Ce(NO_3)_3\cdot6H_2O$, $Gd(NO_3)_3\cdot6H_2O$, $Cu(NO_3)_2\cdot3H_2O$, $La(NO_3)_3\cdot6H_2O$, $Fe(NO_3)_3\cdot9H_2O$, $Ni(NO_3)_2\cdot6H_2O$ were dissolved in deionized water in a beaker. Citric acid was subsequently added into the solution as the complexing agent, with mole (citric acid)/moles (sum of metal cations) = 2.5/1. Ethylene glycol was then added to the solution, with mole (ethylene glycol)/mol (citric acid) = 1.5/1. The solution was stirred at 80 °C until gel formation. The gel was then transferred to a convection oven for drying at 130 °C for 24 h. The dried material was finally calcined in a tube furnace at 750 °C for 6 h with airflow. Mixed CGCO/LNF was synthesized via a high-energy ball mill (JY7124-SWC). Stoichiometric amounts of CGCO and LNF were added into a stainless steel pot. 20 to 30 Al_2O_3 balls were then added into the pot. The pot was then sealed and ball-milled for one hour. After the ball mill, CGCO/LNF was pelletized with 20 MPa pressure and sieved into 90 – 250 μm for reaction tests.

2.2 Characterization of the mixed conductive composites

The formation of crystalline phases of the as-prepared, reduced, and CO_2- or O_2- cycled samples were identified and confirmed by rough X-ray diffraction (XRD) analysis. Diffraction data were collected using a Rigaku SmartLab X-ray diffractometer with Cu-Kα radiation at 40 kV and 44 mA. A stepwise approach with a step size of 0.1° and a residence time of 2.0 s at each step from 25° to 60° angle range (2θ) was used. Detailed refinement scans were conducted with an Empyrean PANalytical XRD with spinner stage. Phase fraction, lattice parameter and lattice oxygen vacancies in CGCO were determined and analyzed via HighScore Plus and Rietveld refinement with a GSAS-2 software[22]. *In-situ* XRD scans were also obtained with the Empyrean PANalytical XRD. The XRD patterns were acquired using similar Cu-Kα radiation operating at 45 kV and 40 mA. A 2θ range

of 25 to 60° was used at a ramp rate of 0.039° holding each step for 0.3 s. The sample was first heated from room temperature to 750 °C at 10°C min^{-1} under 80 ml min^{-1} CO_2/N_2 (6.25 vol%) flow. It was then remained at 750°C and exposed sequentially to CH_4/N_2 (methane POx step, 10 mins) and CO_2/N_2 (CO_2 splitting step, 10 mins) environments for similar 80 ml min^{-1} and 6.25 vol%. A nitrogen purge step for 15-mins was used between the reduction and oxidation steps. Three redox cycles were conducted at the remained temperature and then the sample was cooled down to room temperature at 10°C min^{-1}.

High-resolution transmission electron microscope (TEM) images and EDX mappings were obtained on an S/TEM (FEI Talos F200) operated at 200 kV. The sample was prepared by drop-casting a suspension of the sample in ethanol (anhydrous) on a carbon-coated copper grid and then dried under ambient conditions. Scanning electron microscope (SEM) images were obtained on a Verios 460 (FEI) field-emission electron microscope. The oxygen diffusion coefficient (D) and the relative activation energies of the mixed conductive composites were characterized by an electrical conductivity relaxation (ECR) method. ECR tests were carried out with an in-house system at West Virginia University (WVU). A four-point DC method was used. The measurements were performed in a tube furnace with a fixed gas flow rate of 100 sccm. The conductivity data were obtained using Keithley and fitted with MATLAB. CO-chemisorption was studied using a Quantachrome ChemBET Pulsar instrument. The BET surface areas of the samples were determined using a Micromeritics ASAP 2020 physi/chemisorption system by N_2-adsorption.

2.3 Methane-POx and CO_2 splitting test

For the investigation of the performance in the methane-POx and CO_2 splitting, the reactivity and kinetics of mixed conductive composites CGCO/LNF were studied. Temperature-

programmed reduction (TPR) and isothermal CH_4/CO_2 redox cycles were tested in a thermogravimetric analyzer (TGA). 20 mg of as-prepared sample was placed in the crucible inside TGA. Both the reactant gas and carrier gas were introduced into the chamber from the bottom to minimize the influence of gas convection. The gas flow rate was controlled with a mass flow control (MFC) unit. For TPR tests, the 200 ml min^{-1} CH_4/Ar (5% vol%) was entered the TGA chamber as the temperature increased from 100°C to 850°C. For isothermal redox cycle, the fresh samples were first heated from room temperature to 750°C at a rate of 20 °C min^{-1} and CO_2/Ar (5 vol%) was simultaneously introduced into the chamber at a rate of 200 ml min^{-1}. At reaction temperature, the reactant gas (5 vol% CH_4/Ar) was introduced into the chamber for 5 min in the reduction step. The chamber was purged with Ar for 10 min. Then CO_2/Ar (5 vol% CH_4/Ar) was passed the chamber for 5 min as the oxidation process.

The redox performance was evaluated in a fixed bed configuration using a microreactor (U-shaped quartz tube; 4mm ID) that was vertically placed inside an electric furnace. The composition of the effluent stream was monitored by a quadrupole mass spectrometer (Cirrus 2, MKS). 0.5 g of the redox material (90 to 250 μm) was loaded in the reactor, and quartz wool was packed on both ends of the catalyst to keep the particles in place. The reactor was heated up to reaction temperature in Ar (25 ml min^{-1}). After that, CH_4 (2.8 ml min^{-1}) was introduced for 2 mins followed with Ar purging for 5 mins. After purging, CO_2 (1.0 ml min^{-1}) was introduced for 3 mins as the CO_2 splitting step followed with 5 mins Ar purge prior to the initiation of another redox cycle. In the long-term redox cycle testing, the CO_2 flow rate was set at 1.5 ml min^{-1} to minimize coke formation.

3. Results and discussion
3.1 Phase characterizations of the mixed conductive composites

ARTICLE

Considering the compositional complexity of the mixed oxides selected and their structural differences, it is important to ensure that the two oxides maintain their respective structural integrity in their composite form. A previous study indicated that a dual-phase mixed conductive membrane composed of fluorite structured ceria and perovskites exhibited excellent phase compatibility and mixed ionic-electronic conductivity at ~1000 ^{o}C.[23] However, the phase compatibility between CGCO and LNF has yet to be investigated, especially under redox conditions. **Fig. 2(a)** summarizes the XRD spectra of the as-prepared CGCO, LNF and CGCO/LNF 60/40 samples. Here, x/y (x + y = 100) indicates the weight percentages of the CGCO and LNF components in the composite. As can be seen, fresh CGCO (fluorite) and LNF (orthorhombic perovskite) respectively demonstrated their anticipated structure without phase impurity. Moreover, the composite materials with different compositions (CGCO/LNF 80/20, 40/60, and 20/80) demonstrated distinct fluorite and orthorhombic perovskite phases, confirming the compatibility of CGCO and LNF in the composite structure in **Fig. S1**.

Fig. 2(b) summarizes the XRD patterns of as-prepared, reduced (ending in CH_4 oxidation) and cycled CGCO/LNF 60/40 (ending in CO_2 splitting) at 750°C. Importantly, the XRD patterns of reduced and cycled samples still showed a stable structure with the compatibility of CGCO and LNF. Meanwhile, newly-formed Ni/Fe alloy and La_2O_3 phases were observed in the reduced and cycled sample. The peak of the Ni-Fe phase in the reduced sample is more intensive than that in the cycled sample. The role of these newly formed phases will be further discussed in Section 3.3. Overall, these XRD results indicate that CGCO and LNF remain as the majority phases in the mixed conductive composites after high-temperature annealing and repeated redox cycles, thereby confirming their compatibility and stability for the proposed open-loop hybrid redox process (HRP).
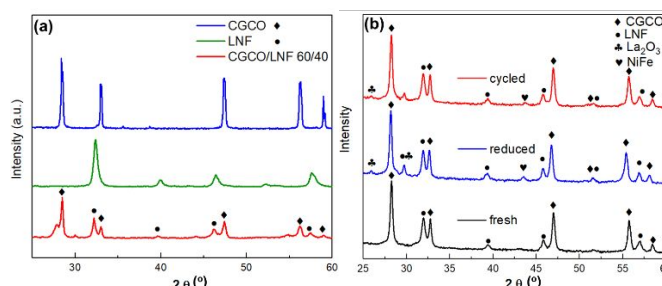
Fig. 2 (a) XRD patterns of as-prepared CGCO, LNF and CGCO/LNF 60/40. (b) XRD patterns of fresh, reduced and cycled CGCO/LNF 60/40.

3.2 Synergistic effects of the mixed conductive composites

Effects on the reducibility of the redox catalysts

Since methane activation is often the limiting factor for low-temperature HRP, CH_4 TPR experiments were first conducted on pure CGCO, LNF and the CGCO/LNF composite (60/40). As illustrated in **Fig. 3**, CGCO is hardly reducible at <800 °C. Although its reduction rate notably increased at >800 °C, we were unable to identify a distinct reduction peak within the temperature range of interest (400 - 850 °C) due to its poor reducibility at lower temperatures. In comparison, LNF exhibited two prominent reduction peaks at 620°C and 680°C. It is noted that CGCO/LNF 60/40 composite also showed two reduction peaks, but at significantly lower temperatures (570°C and 650°C) compared with LNF. This clearly indicates that the reduction of the oxide-based redox catalysts can be facilitated by the mixed CGCO/LNF composite.

In addition, the overall reduction peak areas of CGCO/LNF were significantly larger than those of LNF and CGCO, indicating its potential for higher oxygen-carrying capacity. In addition, coke formation becomes significant for LNF at > 700°C. In comparison, CGCO/LNF exhibited negligible coke formation within the same temperature range. As shown in **Fig. S2(a)**, the weight gain of the LNF for CH_4-TPR starts at > 700°C, showing the coke formation at this temperature. Therefore, the

addition of CGCO to LNF not only enhances the reducibility of the composite material but also improves its coke resistance; both are highly desirable features for HRP redox catalysts. H_2-TPR results, shown in **Fig. S2(b)** further confirm the synergistic effect of the mixed CGCO/LNF composite in terms of its reducibility.
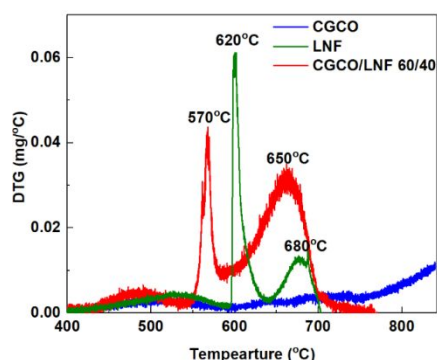
Fig. 3 CH$_4$-TPR of CGCO, LNF and CGCO/LNF 60/40 composite.

Effects on the redox kinetics

The reaction rates of standalone CGCO, LNF and mixed CGCO/LNF composites were studied through TGA under isothermal redox cycles. **Fig. 4(a) and (b)** show the average reduction rates of the redox catalyst during the methane POx step and CO_2 splitting step at 750ºC. As can be seen, the methane POx step is significantly slower than the CO_2-splitting step in all cases, confirming the importance of the redox catalysts' activity for methane conversion. Among these three redox catalysts, CGCO/LNF 60/40 exhibited the highest reduction rate of 0.22 mg min^{-1} and oxidation rate of 1.09 mg min^{-1}, respectively. To compare, the reduction and oxidation rate of CGCO were as lower as 0.04 and 0.8 mg min^{-1}; and LNF were 0.08 and 1.04 mg min^{-1}. Additional kinetic data at reaction temperatures ranging from 600ºC to 750ºC are provided in **Fig. S3.** Overall, CGCO/LNF consistently exhibited superior activity over CGCO and LNF. This confirms the synergistic effect between the two phases. In addition, the reaction rate of the CO_2-splitting step was nearly 4 times that of the methane POx step, indicating that methane activation is the rate-limiting step. The faster redox kinetics of the CGCO/LNF composite also resulted in a higher overall lattice oxygen extraction amount of oxygen-carrying capacity. For instance, 2.5-4 w.t.% oxygen capacity was observed between 600 and 750 °C. In comparison, LNF and CGCO exhibited oxygen capacities of 1 w.t.% and 0.6 w.t.% respectively[24].

The kinetic data obtained from TGA tests were further analyzed through an isoconversional kinetic method for gas-solid reactions[25], with further details provided in the ESI. The Arrhenius plots of the redox catalysts during the methane POx step (**Fig. S4**) indicate that incorporating CGCO and LNF in a composite form led to decreased activation energy. CGCO showed activation energy of 122.5 kJ mol^{-1} (1.27 eV)[26], LNF activation energy was 1.07 eV, whereas that for CGCO/LNF 60/40 was 0.70 eV[27]. Overall, the reaction rate data and apparent activation energy clearly demonstrate the kinetic advantages of the CGCO/LNF over its individual constituents.
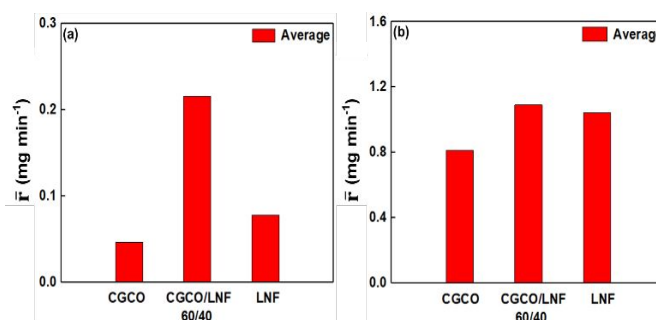
Fig. 4 The average rates of reaction for CGCO, LNF, and CGCO/LNF 60/40 in 5% CH$_4$/Ar at 750ºC over (a) the methane POx step; (b) the CO_2 splitting step.

Effects on the redox performance in HRP

To demonstrate the performance of the redox catalysts in HRP, methane-POx and CO_2 splitting experiments were conducted in a fixed-bed reactor. **Fig. 5(a)** compares the catalyst performance of standalone CGCO, LNF and CGCO/LNF 60/40 at 750 °C. Standalone CGCO was nearly inactive for methane activation at 750ºC, e.g. less than 5% methane and CO_2 conversions with less than 0.1

w.t.%. active oxygen being extracted. LNF was more active than CGCO but both methane and CO_2 conversions were still limited to <35%. In comparison, CGCO/LNF 60/40 exhibited a synergistic effect and the catalyst performance was significantly improved, with both increased conversion and CO selectivity. More than 90% of both methane and CO_2 conversions were obtained, with ~0.6 w.t.% oxygen extracted. This represents a 6-fold increase compared to CGCO and a 3-fold increase compared to LNF (**Fig. S5**). High CO yield (96%) and an ideal syngas composition ($H_2/CO = 2$) were also obtained for CGCO/LNF 60/40.

Due to the limited size of the packed bed and gas dispersion, the degrees of reduction and oxidation of the redox catalysts are limited in order to obtain high methane and CO_2 conversions (before breakthroughs occur). As such, the oxygen capacities demonstrated in packed bed studies are notably lower than those from TGA.

Fig. 5(b) shows the temperature effect on the reactivity of CGCO/LNF 60/40. As can be seen, significant methane conversion was observed at 650°C or higher. Among the temperatures investigated, 750°C was deemed to be a desirable operating temperature, with both satisfactory

CH_4/CO_2 conversions and syngas selectivity. Higher temperatures (e.g., 800°C and 850°C) exhibited higher CH_4/CO_2 conversions but with coke formation as indicated by higher H_2/CO ratios (**Fig. S6**). It is noted that H_2/CO was 2.5 for the standalone LNF and also for the CGCO/LNF 20/80, indicating that the LNF was prone to coke formation. In comparison, CGCO/LNF samples with higher than 20 w.t.% CGCO exhibited excellent coke resistance.

The impact of CGCO/ LNF ratios is summarized in **Fig. 5(c)**. Close to 90% methane conversion was obtained for all the mixed conductive composites. CGCO/LNF of 60/40 weight ratio was the best performing redox catalyst, showing the highest CH_4/CO_2 conversion (90%) and CO selectivity (96%). The stability of CGCO/LNF 60/40 during long-term CH_4-PO_x and CO_2 splitting redox cycles was also tested and the results are shown in **Fig. 5(d)**. Methane conversion remained at 87% with active oxygen extraction at 0.47 w.t. % for each cycle. This oxygen capacity is sufficient in the proposed methane-POx/CO_2 splitting HRP scheme and is much higher than those of CGCO (0.1 w.t. %) and LNF (0.25 w.t. %).
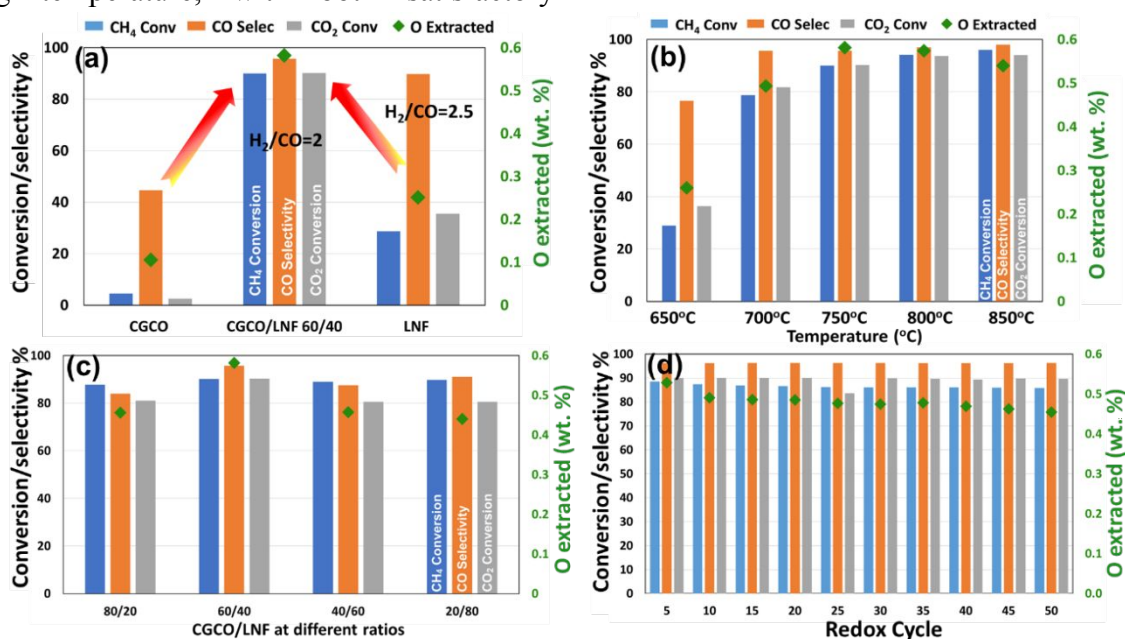
Fig. 5 (a) The reactivity of CGCO, LNF, CGCO/LNF (at 750°C); (b) Effect of temperature on the activity of CGCO/LNF 60/40; (c) Effect of CGCO/ LNF ratios; (d) Long term stability of CGCO/LNF 60/40.

3.3 Mechanistic investigations

Synergistic effects on bulk redox properties

HRP is a redox process with dynamic change on redox catalyst phases, lattice oxygen vacancy and surface structure. Understanding these dynamic changes can offer critical mechanistic insights on redox catalyst performance[28]. The *in-situ* XRD under methane-PO_x/CO_2 splitting redox cycles at 750°C was conducted. **Fig. 6(a)** shows the XRD patterns of CGCO/LNF 60/40 during one redox cycle. Detailed phase assignments are in **Fig. 6(b)**. It was observed that both CGCO and LNF contribute to the overall lattice oxygen extraction but with different mechanisms. CGCO contributes to the lattice oxygen extraction by oxygen vacancy formation during the reduction step, as indicated by the peak shift of (111) plane of CGCO (by 0.04°). Meanwhile, LNF contributes to the lattice oxygen extraction by partial decomposition to La_2O_3 and a bimetallic Ni-Fe phase. It is also noted that the crystallite size of Ni-Fe in the reduced composites is 25.2 nm, which is smaller than that of Ni-Fe (18.3 nm) in the reoxidized sample, confirming the dynamic exsolution of the Ni-Fe phase. That is, Ni-Fe and La_2O_3 are partially incorporated back into the LNF phase during the CO_2-splitting step. To compare, standalone CGCO and LNF showed minimal change between reduced and oxidized states (**Fig. S7**).

Rietveld refinement was conducted on CGCO, LNF and the composite redox catalyst in both oxidized and reduced states and the lattice oxygen extraction were calculated based on lattice oxygen stoichiometry (δ) of $Ce_{0.85}Gd_{0.1}Cu_{0.05}O_{2-\delta}$ and La_2O_3/$LaNi_{0.35}Fe_{0.65}O_3$ phase molar ratio (**Fig. S8**). The calculated lattice oxygen extraction was comparable with experimental results from TGA (**Fig. S3**). Detailed information concerning Rietveld refinement is shown in **Table S1**. As shown in **Fig. 6(c)**, significantly more lattice oxygen vacancies were formed from CGCO in the composite material than standalone CGCO, as indicated by the more

than a 6-fold increase of lattice oxygen capacity. Simultaneously, LNF was more deeply reduced to La_2O_3 and Ni-Fe than standalone LNF. These XRD observations correspond well with the synergistic effects observed in the previous section.
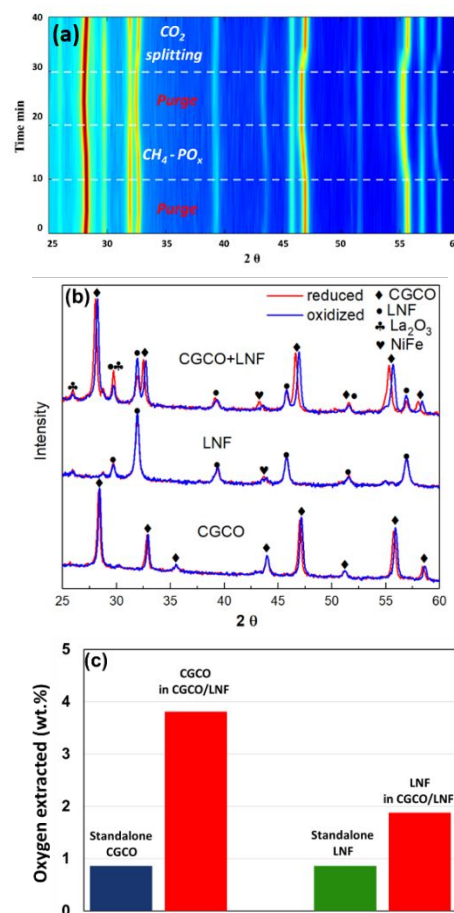
Fig. 6 (a) *In-situ* XRD patterns of CGCO/LNF 60/40 for the redox cycle; (b) *In-situ* XRD patterns of CGCO/LNF 60/40 at 750°C for reduced and oxidized materials. (c) Lattice oxygen extraction from standalone CGCO, LNF and CGCO, LNF in composite phase (CGCO/LNF 60/40) based on Rietveld refinement.

The electrical conductivity relaxation (ECR) technique was used to determine the lattice oxygen migration rates of CGCO, LNF and CGCO/LNF 60/40 and the results are summarized in **Fig. 7**. The activation energies (Ea) were calculated based on the diffusion coefficient (D) measurements. It was observed that CGCO and LNF exhibited similar

activation energies for lattice oxygen migration and LNF (1.36 eV) was slightly smaller than CGCO (1.03 eV). On the other hand, CGCO/LNF 60/40 showed much lower activation energy as 0.43 eV. This indicated that lattice oxygen migration in CGCO/LNF 60/40 was significantly facilitated for the synergistic effect of the mixed conductive composites. It is noted that the energy barrier for oxygen conduction in CGCO/LNF is significantly lower than standalone CGCO and LNF, which shows a consistent trend with their apparent activation energies for methane POx.
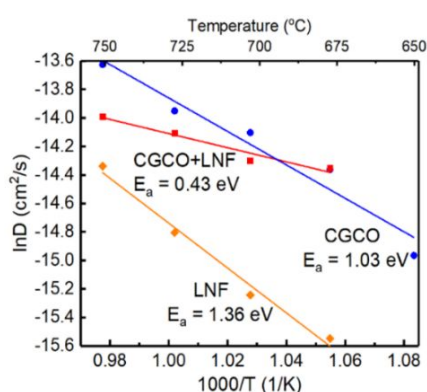
Fig. 7 Arrhenius plots of CGCO, LNF, and CGCO/LNF 60/40 based on ECR measurements.

Synergistic effects for surface catalytic properties.

TEM and EDX images were obtained on reduced CGCO/LNF (CGCO/LNF=60/40) ending in the methane-POx step (**Fig. 8**). As can be seen, reduced CGCO/LNF exhibited isolated islands of bimetallic Ni-Fe particles with a diameter ranging between 20 and 40 nm. TEM images also showed segregated phases of Ni-Fe, CGCO and LNF, as indicated by the lattice spacing from their (111), (111) and (121) planes, respectively. Meanwhile, oxidized CGCO/LNF ending in the CO_2 splitting step showed a more homogeneous distribution of all the elements. This is consistent with *in-situ* XRD results, where the exsolution of bimetallic Ni-Fe was observed during the methane-POx step. In addition, the SEM images of the CGCO/LNF 60/40 fresh and cycled were shown in **Fig. S10**. These mappings indicated that the morphology of the CGCO/LNF 60/40 remained consistent and the structure of the mixed CGCO/LNF 60/40 composite was stable after redox cycles.
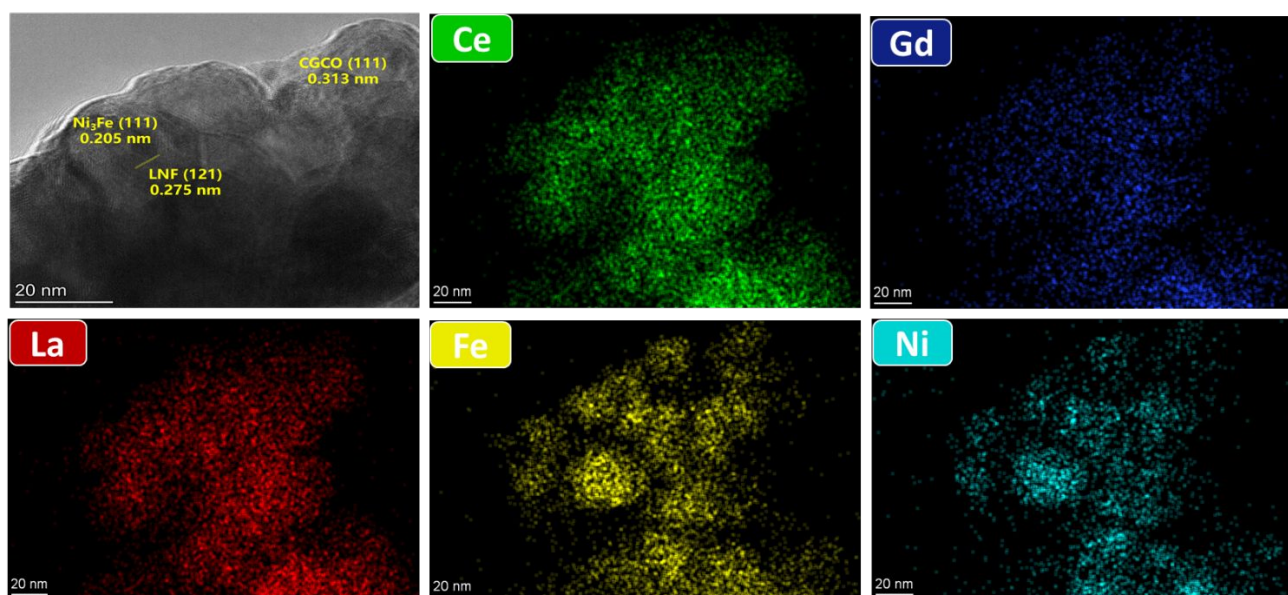
Fig. 8 The TEM and EDX mappings of reduced CGCO/LNF (CGCO/LNF=60/40)

CO chemisorption was conducted on reduced, standalone CGCO, LNF and CGCO/LNF composite to further quantify the bimetallic Ni-Fe surface sites, as summarized in **Table S2**. Total CO adsorption for reduced CGCO/LNF was 1.21×10^{-5} mol g^{-1} and much higher than that of both reduced standalone CGCO (4.01×10^{-6} mol g^{-1}) and LNF (1.10×10^{-6} mol g^{-1}). The results indicate that reduced CGCO/LNF exhibited significantly more Ni-Fe surface sites than reduced LNF, further confirming its superior catalytic activity. In terms of surface area, CGCO/LNF exhibited a higher specific surface area (17.09 m^2 g^{-1}) than LNF (8.35 m^2 g^{-1}) and CGCO (4.02 m^2 g^{-1}) (**Table S3**). The higher surface area was probably due to the high-energy ball milling during its preparation.

The characterization results above indicate that the bimetallic Ni-Fe particles, formed during the reduction of CGCO/LNF composite, are likely to be responsible for the composite samples' surface catalytic activity for methane activation. The role of bimetallic Ni-Fe was further confirmed under methane-PO_x/Air re-oxidation redox cycles. As shown in **Fig. 9(a)**, CGCO/LNF ending in air re-oxidation step exhibited much lower activity for methane conversion. This corresponds well with XRD results in **Fig. 9(b)**, which confirms the absence of Ni-Fe phase in CGCO/LNF ending in the air re-oxidation. This is understandable since Ni-Fe exsoluted from LNF would be fully incorporated back into the LNF structure under the strong oxidizing environment in the presence of O_2. The presence of exsoluted Ni-Fe on the surface of CGCO/LNF under methane-PO_x/CO_2 redox cycles is hence responsible for the surface catalytic activity of the composite sample. Furthermore, the superior catalytic activity for methane activation, coupled with the higher lattice oxygen conductivity of the composite redox catalyst, would in turn enhance the lattice oxygen extraction from both the LNF and CGCO phases.
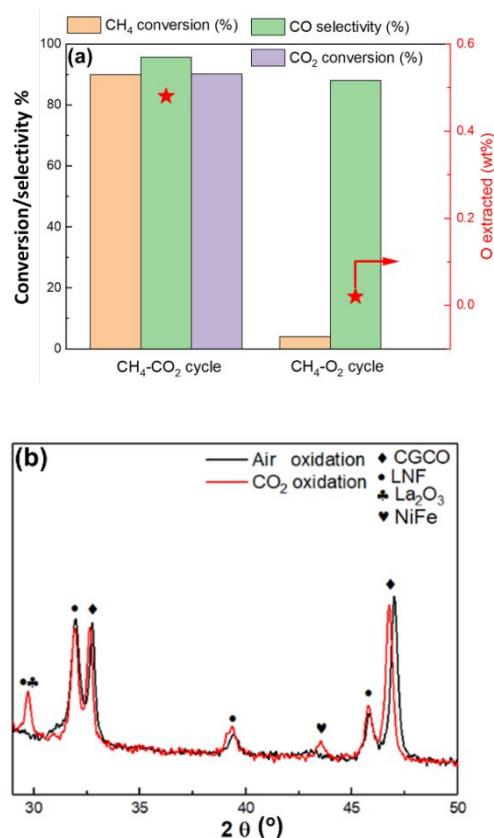
Fig. 9 (a) Comparison of reaction performance of CGCO-LNF with CH_4-CO_2 redox cycle and CH_4-O_2 redox cycle; (b) the XRD patterns of CGCO/LNF 60/40 ended in CH_4-CO_2 redox cycle and CH_4-O_2 redox cycle.

Based on the characterization results above, the synergistic effects of CGCO/LNF and the schematic of the reaction mechanism are illustrated in **Fig. 10**. The phase cooperation between CGCO and LNF in the CGCO/LNF composites facilitated lattice oxygen migration and promoted the formation of bimetallic Ni-Fe surface sites. Meanwhile, the Ni-Fe acted as active sites for methane activation and helped to release more lattice oxygen from both LNF and CGCO phases in the composites. As a result, high methane conversion, CO selectivity and high lattice oxygen extraction were obtained on CGCO/LNF in chemical looping methane-PO_x/CO_2-splitting redox cycles. **Table S4** summarizes the performance of the redox catalyst in this study and those reported in recent publications.

ARTICLE
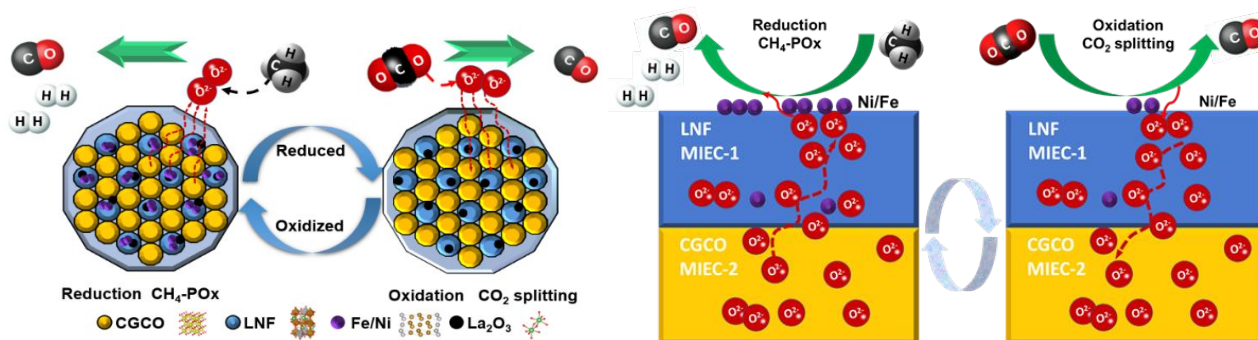
Fig. 10 Schematic of reaction mechanism on mixed conductive composite CGCO/LNF.

4. Conclusions

A rationalized strategy to design effective, PGM free redox catalysts for "low temperature", redox-based CO_2 splitting and methane partial oxidation were proposed and validated. Specifically, composites of two mixed-conductive oxides with distinct structures, i.e., $Ce_{0.85}Gd_{0.1}Cu_{0.05}O_{2-\delta}$ (CGCO) and $LaNi_{0.35}Fe_{0.65}O_3$ (LNF), were found to be highly effective. Fixed bed experiments of CGCO/LNF 60/40 demonstrated up to 90% CO_2 conversion (in CO_2-splitting) and 96% syngas selectivity with 90% methane conversion (in methane POx) at 750°C, significantly higher than those of standalone LNF and CGCO. Detailed characterizations of the redox catalysts reveal the underlying mechanism for the synergistic effects of the LNF and CGCO phases: (i) ECR measurements indicate that simultaneous presence of both phases in the composite resulted in significantly lowered activity for lattice oxygen conduction (0.43 eV *vs.* 1.36 and 1.03 eV for individual phases); (ii) facile lattice oxygen removal facilitated by the enhanced oxygen conductivity in turn promotes the reversible exsolution of active transition metal nanoparticles (Ni-Fe alloy) on the oxide surface, acting as active sites for methane activation as confirmed by *in-situ* XRD, TEM, and CO-chemisorption. Resulting from these synergistic effects, the composite redox catalysts exhibit significantly lowered activation energy for methane activation (0.70 eV for

CGCO/LNF 60/40) and superior redox activity at 600 - 750°C, excellent resistance towards coke formation, and stability over repeated HRP redox cycles. As such, the mixed conductive composites have the potential to be a suitable candidate for low temperature thermochemical CO_2 splitting and syngas generation.

Conflicts of interest

There are no conflicts to declare.

Acknowledgments

References

1. IPCC, IPCC special report on carbon dioxide capture and storage. *Cambridge(UK): Cambridge University Press* **2005**.

2. Newell, R. G.; Raimi, D.; Aldana, G., Global Energy Outlook 2019: The Next Generation of Energy. **2019**.

3. (a) Agency, I. E., World Energy Outlook 2012. *Paris(France):OECD/IEA* **2012**; (b) Administration, U. S. E. I., International Energy Outlook 2011. **2011**; (c) U.S. Energy Information Administration forecasts. **2011 (accessed October 2012)**.

4. (a) Boot-Handford, M. E.; Abanades, J. C.; Anthony, E. J.; Blunt, M. J.; Brandani, S.; Mac Dowell, N.; Fernández, J. R.; Ferrari, M.-C.; Gross, R.; Hallett, J. P.; Haszeldine, R. S.; Heptonstall, P.; Lyngfelt, A.; Makuch, Z.; Mangano, E.; Porter, R. T. J.; Pourkashanian, M.; Rochelle, G. T.; Shah, N.; Yao, J. G.; Fennell, P. S., Carbon capture and storage update. *Energy Environ. Sci.* **2014,** *7* (1), 130-189; (b) Bhatia, S., Carbon capture and storage: Solution or a challenge. *Hydrocarb Process* **2008,** *87* (11), 99-104.

5. Zhao, G.; Huang, X.; Wang, X.; Wang, X., Progress in catalyst exploration for heterogeneous CO2 reduction and utilization: a critical review. *J. Mater. Chem. A* **2017,** *5* (41), 21625-21649.

6. Peter, S. C., Reduction of CO2 to Chemicals and Fuels: A Solution to Global Warming and Energy Crisis. *Acs Energy Lett* **2018,** *3* (7), 1557-1561.

7. Kuhl, K. P.; Cave, E. R.; Abram, D. N.; Jaramillo, T. F., New insights into the electrochemical reduction of carbon dioxide on metallic copper surfaces. *Energy & Environmental Science* **2012,** *5* (5), 7050-7059.

8. Halmann, M., Photoelectrochemical reduction of aqueous carbon dioxide on p-type gallium phosphide in liquid junction solar cells. *Nature* **1978,** *275* (5676), 115.

9. Hou, J.; Cheng, H.; Takeda, O.; Zhu, H., Three‐Dimensional Bimetal‐Graphene‐Semiconductor Coaxial Nanowire Arrays to Harness Charge Flow for the Photochemical Reduction of Carbon Dioxide. *Angewandte Chemie International Edition* **2015,** *54* (29), 8480-8484.

10. (a) Chueh, W. C.; Falter, C.; Abbott, M.; Scipio, D.; Furler, P.; Haile, S. M.; Steinfeld, A., High-Flux Solar-Driven Thermochemical Dissociation of CO2 and H2O Using Nonstoichiometric Ceria. *Science* **2010,** *330* (6012), 1797-1801; (b) Kubicek, M.; Bork, A. H.; Rupp, J. L. M., Perovskite oxides – a review on a versatile material class for solar-to-fuel conversion processes. *Journal of Materials Chemistry A* **2017,** *5* (24), 11983-12000; (c) Al-Shankiti, I.; Ehrhart, B. D.; Weimer, A. W., Isothermal redox for H2O and CO2 splitting – A review and perspective. *Solar Energy* **2017,** *156*, 21-29; (d) Palcheva, R.; Olsbye, U.; Palcut, M.; Rauwel, P.; Tyuliev, G.; Velinov, N.; Fjellvåg, H. H., Rh promoted La0.75Sr0.25(Fe0.8Co0.2)1−xGaxO3-δ perovskite

catalysts: Characterization and catalytic performance for methane partial oxidation to synthesis gas. *Applied Surface Science* **2015,** *357*, 45-54; (e) Bork, A. H.; Povoden-Karadeniz, E.; Rupp, J. L. M., Modeling Thermochemical Solar-to-Fuel Conversion: CALPHAD for Thermodynamic Assessment Studies of Perovskites, Exemplified for (La,Sr)MnO3. *Advanced Energy Materials* **2017,** *7* (1); (f) Arifin, D.; Aston, V. J.; Liang, X. H.; McDaniel, A. H.; Weimer, A. W., CoFe2O4 on a porous Al2O3 nanostructure for solar thermochemical CO2 splitting. *Energy & Environmental Science* **2012,** *5* (11), 9438-9443; (g) Muhich, C.; Steinfeld, A., Principles of doping ceria for the solar thermochemical redox splitting of H2O and CO2. *Journal of Materials Chemistry A* **2017,** *5* (30), 15578-15590.

11. (a) Steinfeld, A., High-temperature solar thermochemistry for CO2 mitigation in the extractive metallurgical industry. *Energy* **1997,** *22* (2-3), 311-316; (b) Haribal, V. P.; Wang, X.; Dudek, R.; Paulus, C.; Turk, B.; Gupta, R.; Li, F., Modified Ceria for "Low‐Temperature" CO2 Utilization: A Chemical Looping Route to Exploit Industrial Waste Heat. *Advanced Energy Materials* **2019**, 1901963; (c) Zhang, J.; Haribal, V.; Li, F., Perovskite nanocomposites as effective CO2-splitting agents in a cyclic redox scheme. *Sci Adv* **2017,** *3* (8), e1701184; (d) Zhu, X.; Imtiaz, Q.; Donat, F.; Müller, C. R.; Li, F., Chemical looping beyond combustion – a perspective. *Energy & Environmental Science* **2020**.

12. (a) Steinfeld, A.; Frei, A.; Kuhn, P.; Wuillemin, D., SOLAR THERMAL PRODUCTION OF ZINC AND SYNGAS VIA COMBINED ZNO-REDUCTION AND CH4-REFORMING PROCESSES. *International Journal of Hydrogen Energy* **1995,** *20* (10), 793-804; (b) Ishida, M.; Jin, H. G., A New Advanced Power-Generation System Using Chemical-Looping Combustion. *Energy* **1994,** *19* (4), 415-422.

13. (a) Tang, M.; Xu, L.; Fan, M., Progress in oxygen carrier development of methane-based chemical-looping reforming: A review. *Applied Energy* **2015,** *151*, 143-156; (b) Kang, D.; Lim, H. S.; Lee, M.; Lee, J. W., Syngas production on a Ni-enhanced Fe2O3/Al2O3 oxygen carrier via chemical looping partial oxidation with dry reforming of methane. *Applied Energy* **2018,** *211*, 174-186.

14. (a) Bhavsar, S.; Najera, M.; Veser, G., Chemical Looping Dry Reforming as Novel, Intensified Process for CO2 Activation. *Chem Eng Technol* **2012,** *35* (7), 1281-1290; (b) Najera, M.; Solunke, R.; Gardner, T.; Veser, G., Carbon capture and utilization via chemical looping dry reforming. *Chem Eng Res Des* **2011,** *89* (9), 1533-1543.

15. AmeyMore, S. B., and Gçtz Veser, Iron–Nickel Alloys for Carbon Dioxide Activation by Chemical Looping Dry Reforming of Methane. *Energy Technology* **2015,** *4*, 1147–1157.

16. (a) Lofberg, A.; Guerrero-Caballero, J.; Kane, T.; Rubbens, A.; Jalowiecki-Duhamel, L., Ni/CeO2 based catalysts as oxygen vectors for the chemical looping dry reforming of methane for syngas production. *Applied Catalysis B-Environmental* **2017,** *212*, 159-174; (b) Galvita, V. V.; Poelman, H.; Detavernier, C.; Marin, G. B., Catalyst-assisted chemical looping for CO2 conversion to CO. *Applied Catalysis B: Environmental* **2015,** *164*, 184-191.

17. (a) Das, S.; Ashok, J.; Bian, Z.; Dewangan, N.; Wai, M.; Du, Y.; Borgna, A.; Hidajat, K.; Kawi, S., Silica–Ceria sandwiched Ni core–shell catalyst for low temperature dry reforming of biogas: Coke resistance and mechanistic insights. *Applied Catalysis B: Environmental* **2018,** *230*, 220-236; (b) Zhang, J.; Li, F., Coke-resistant Ni@SiO2 catalyst for dry reforming of methane. *Applied Catalysis B: Environmental* **2015,** *176-177*, 513-521.

18. Imanieh, M. H.; Rad, M. H.; Nadarajah, A.; González-Platas, J.; Rivera-López, F.; Martín, I. R., Novel perovskite ceramics for chemical looping combustion application. *Journal of CO2 Utilization* **2016,** *13*, 95-104.

19. (a) Xing, Z.; Kongzhai, L.; M, N. L.; Fanxing, L., Perovskites as geo-inspired oxygen storage materials for chemical looping and three-way catalysis – a perspective. *ACS Catalysis*, acscatal.8b01973-; (b) Galinsky, N. L.; Huang, Y.; Shafiefarhood, A.; Li, F., Iron Oxide with Facilitated O_2–Transport for Facile Fuel Oxidation and CO_2Capture in a Chemical Looping Scheme. *ACS Sustainable Chemistry & Engineering* **2013,** *1* (3), 364-373.

20. Michalsky, R.; Neuhaus, D.; Steinfeld, A., Carbon Dioxide Reforming of Methane using an Isothermal Redox Membrane Reactor. *Energy Technology* **2015,** *3* (7), 784-789.

21. (a) Shafiefarhood, A.; Zhang, J.; Neal, L. M.; Li, F., Rh-promoted mixed oxides for "low-temperature" methane partial oxidation in the absence of gaseous oxidants. *Journal of Materials Chemistry A* **2017,** *5* (23), 11930-11939; (b) Mishra, A.; Shafiefarhood, A.; Dou, J.; Li, F., Rh promoted perovskites for exceptional "low temperature" methane conversion to syngas. *Catalysis Today* **2019**.

22. Toby, B. H.; Von Dreele, R. B., GSAS-II: the genesis of a modern open-source all purpose crystallography software package. *Journal of Applied Crystallography* **2013,** *46* (2), 544-549.

23. Fang, W.; Liang, F.; Cao, Z.; Steinbach, F.; Feldhoff, A., A mixed ionic and electronic conducting dual-phase membrane with high oxygen permeability. *Angew Chem Int Ed Engl* **2015,** *54* (16), 4847-50.

24. Khawam, A.; Flanagan, D. R., Solid-State Kinetic Models: Basics and Mathematical Fundamentals. *The Journal of Physical Chemistry B* **2006,** *110* (35), 17315-17328.

25. Vyazovkin, S.; Burnham, A. K.; Criado, J. M.; Pérez-Maqueda, L. A.; Popescu, C.; Sbirrazzuoli, N., ICTAC Kinetics Committee recommendations for performing kinetic computations on thermal analysis data. *Thermochimica Acta* **2011,** *520* (1), 1-19.

26. Ramírez-Cabrera, E.; Atkinson, A.; Chadwick, D., Catalytic steam reforming of methane over $Ce_{0.9}Gd_{0.1}O_2$–x. *Applied Catalysis B: Environmental* **2004,** *47* (2), 127-131.

27. Dai, X.; Cheng, J.; Li, Z.; Liu, M.; Ma, Y.; Zhang, X., Reduction kinetics of lanthanum ferrite perovskite for the production of synthesis gas by chemical-looping methane reforming. *Chemical Engineering Science* **2016,** *153*, 236-245.

28. Neal, L. M.; Shafiefarhood, A.; Li, F., Dynamic Methane Partial Oxidation Using a $Fe_2O_3@La_{0.8}Sr_{0.2}FeO_3$-δ Core–Shell Redox Catalyst in the Absence of Gaseous Oxygen. *ACS Catalysis* **2014,** *4* (10), 3560-3569.